

Numerical Simulation of Nonlinear Mesoscale Circulations Induced by the Thermal Heterogeneities of Land Surface

JINGFENG WANG, ELFATIH A. B. ELTAHIR, AND RAFAEL L. BRAS

Department of Civil and Environmental Engineering, Massachusetts Institute of Technology, Cambridge, Massachusetts

(Manuscript received 10 October 1996, in final form 3 July 1997)

ABSTRACT

Mesoscale circulations forced by a random distribution of surface sensible heat flux have been investigated using a three-dimensional numerical model. The complex land surface is modeled as a homogeneous random field characterized by a spectral distribution. Standard deviation and length scale of the sensible heat flux at the surface have been identified as the important parameters that describe the thermal variability of land surface. The form of the covariance of the random surface forcing is not critical in driving the mesoscale circulation. The thermally induced mesoscale circulation is significant and extends up to about 5 km when the atmosphere is neutral. It becomes weak and is suppressed when the atmosphere is stable. The mesoscale momentum flux is much stronger than the corresponding turbulent momentum flux in the neutral atmosphere, while the two are comparable in the stable atmosphere. The mesoscale heat flux has a different vertical profile than turbulent heat flux and may provide a major heat transport mechanism beyond the planetary boundary layer. The impact of synoptic wind on the mesoscale circulations is relatively weak. Nonlinear advection terms are responsible for momentum flux in the absence of synoptic wind.

1. Introduction

Atmospheric circulations induced by differential heating is an important mesoscale process. One well-known example is the sea breeze driven by the thermal contrast between land and water. Such a sharp contrast in surface heating is less common over continental regions where the thermal heterogeneity of the land surface results from variable vegetation cover, soil properties, and/or soil moisture distribution. Nevertheless, the gradual variation of land surface properties may still be sufficient to drive a land breeze under favorable atmospheric conditions. This type of mesoscale processes is potentially important for the transport of momentum, heat, and moisture from the surface, and will be the focus of this paper.

Substantial progress in understanding the role of land surface in the development of thermally induced mesoscale circulations has been achieved in the last 20 years. Linear analytical models (e.g., Rotunno 1983; Dalu and Pielke 1989) predict significant mesoscale circulation under the conditions of idealized land surface heterogeneities. Mesoscale fluxes comparable to turbulent fluxes have been found using a linear model

(Dalu and Pielke 1993). Nonlinear analysis of mesoscale circulations has been conducted with the help of numerical models. A good source of references on this topic can be found in a monograph by Pielke (1984). The numerical simulations (Pielke 1974; Mahrer and Pielke 1977; Segal et al. 1989; Huss and Feliks 1981; Ookouchi et al. 1984; Segal et al. 1986; Mahfouf et al. 1987; Yan and Anthes 1988; Segal et al. 1988; Avissar and Pielke 1989; André et al. 1990; Xian and Pielke 1991; Pielke et al. 1991; Avissar and Chen 1993; Li and Avissar 1994; Lynn et al. 1995a,b; and others) have suggested that significant mesoscale circulations comparable to the sea breeze can be induced when the land surface is covered by warm-cool patches or strips of a variety of sizes. Although the regular distribution of land surface assumed in previous studies is somewhat unrealistic, these works have improved our knowledge of thermally induced mesoscale circulations and provide a good starting point for further exploration.

In contrast to the idealized patterns of the land surface considered in the aforementioned analytical and numerical studies, natural landscapes often manifest complex distributions of surface properties over mesoscale domains. Sun and Mahrt (1994) have shown that NDVI, the *normalized difference of vegetation index* defined as the difference of the reflectance at the near-infrared region and visible region divided by the sum of the two, is highly correlated with sensible heat flux at the surface and hence may be used as a proxy for the latter. Satellite images (an example is shown in Fig. 1) from AVHRR

Corresponding author address: Dr. Jingfeng Wang, Department of Civil and Environmental Engineering, Massachusetts Institute of Technology, 48-320, Ralph M. Parsons Laboratory, Cambridge, MA 02139-4307.
E-mail: jfwang@mit.edu

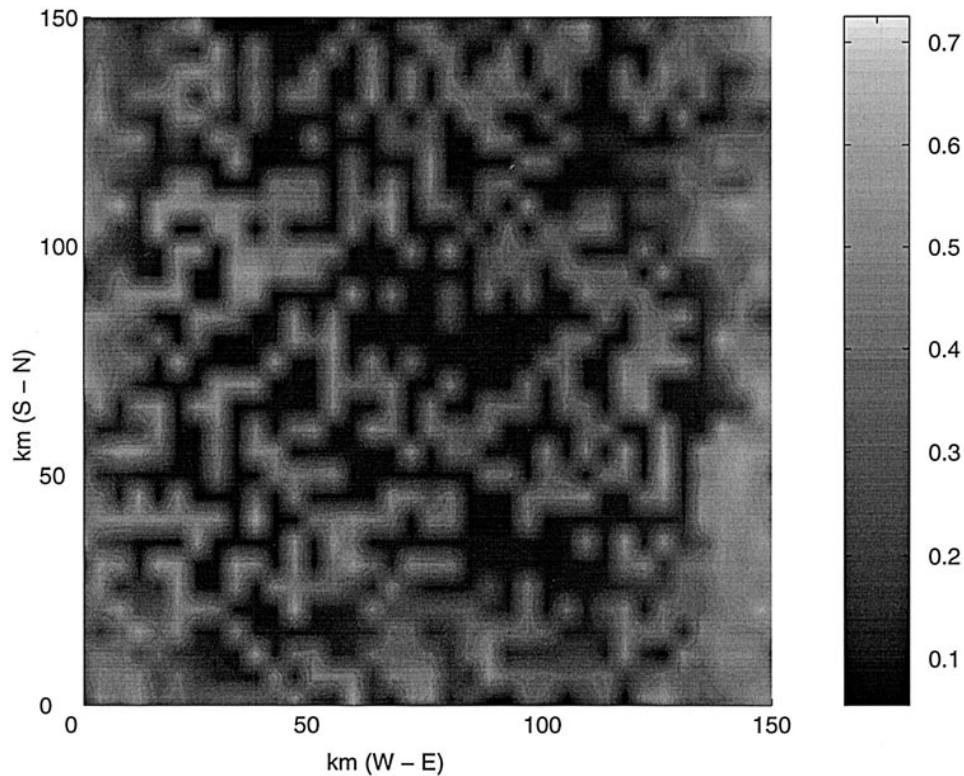


FIG. 1. Vegetation index (NDVI) over Kansas (composite data of 1–10 July 1992) from 1-km AVHRR satellite observations. The image domain is centered at 39°N, 98°W.

observations (e.g., Eidenshink 1992) illustrate complex or random patterns of NDVI over the surface with a wide range of length scales. Wang et al. (1996) recently proposed a stochastic linear theory to evaluate the impact of land surface heterogeneity of random distribution on mesoscale circulations. Assuming a homogeneous random field, an analytical ensemble solution of the governing flow equations was obtained and utilized to derive the formulas of the flow intensity and mesoscale fluxes. The flow intensity is shown to be proportional to the standard deviation of turbulent sensible heat flux over the land surface, and the mesoscale fluxes of momentum, heat, and moisture are proportional to the variance. This linear theory also suggests that atmospheric stability and synoptic wind strongly inhibit the development of thermally induced flow. Under a favorable environment (neutral stratification and zero/slight synoptic wind) significant momentum and heat fluxes were predicted by the linear theory.

The accuracy of the linear theory in describing mesoscale circulations depends critically on relative magnitudes and the importance of omitted nonlinear components of the mesoscale system. Since a general analytical approach for nonlinear analysis is not currently available, we used a numerical mesoscale model to further assess the importance of mesoscale circulations forced by a homogeneous random field of sensible heat flux at the surface. The spatial distribution of turbulent

sensible heat flux over the land surface is generated according to the spectrum of the random field. Realistic values of the key parameters characterizing the spectrum are chosen to be consistent with observations. Different stability and synoptic wind conditions were also tested to investigate their roles in determining the spatial-temporal distribution of mesoscale kinetic energy, momentum flux, and heat flux.

In the following, we first briefly describe the natural variability of land surface in section 2. The design of the numerical experiments is given in section 3 followed by the discussion of results in section 4. A comparison of the numerical simulations with the linear theory of Wang et al. (1996) is the theme of section 5. The conclusions are presented in section 6.

2. Observed variability of surface sensible heat flux

Dry convection in the atmosphere is forced by the diabatic heating resulting from the *turbulent sensible heat flux* (TSHF) emitted from the land surface. Several field experiments provide useful information about the spatial distribution of TSHF over mesoscale domains. In the region of the California Ozone Deposition Experiment, where the land was covered by crops and bare soil, a difference of $\sim 200 \text{ W m}^{-2}$ in TSHF over a distance about 10 km was evident from aircraft measure-

TABLE 1. Vertical grid points in the numerical model.

Level	Height z (m)
1	0
2	53
3	156
4	309
5	513
6	768
7	1073
8	1428
9	1826
10	2257
11	2712
12	3183
13	3665
14	4154
15	4647
16	5143
17	5640
18	6138
19	6637
20	7136

ments (Sun and Mahrt 1994). Satellite images (from 1 km AVHRR) of this region reveal the existence of such land surface heterogeneity over a much larger surrounding area. At the site of the Boardman Regional Flux Experiment near Boardman, Oregon, where the experiment domain consists of mixed steppe and irrigated

farm areas of irregular shapes, some 300 W m^{-2} variation in TSHF with length scales of 10 km or more was documented by Doran et al. (1995). Field data collected from HAPEX-MOBILHY (André et al. 1990) point to a difference in TSHF of around 100 W m^{-2} across 30 km due to variations in canopy (Mahrt and Ek 1993). Significant variability in TSHF has also been observed within the relatively small experimental area at the FIFE site (e.g., Desjardins et al. 1992). The variability and length scale of TSHF over land surface prescribed in our numerical simulations are consistent with these observations.

3. Numerical model

The numerical model used in this study is the updated three-dimensional CLARK model (version G2TC38) developed at the National Center for Atmospheric Research. A detailed description of this model is given by Clark (1977), hence is not repeated here.

The model is nonhydrostatic and can be forced by a prescribed TSFH over the land surface. The atmosphere is assumed to be dry. The simulation domain is a $200 \text{ km} \times 200 \text{ km}$ area. The atmosphere is divided into 20 vertical levels with variable increments (see Table 1). The horizontal resolution is either 5 or 10 km depending on the length scale of the TSHF at the surface. The

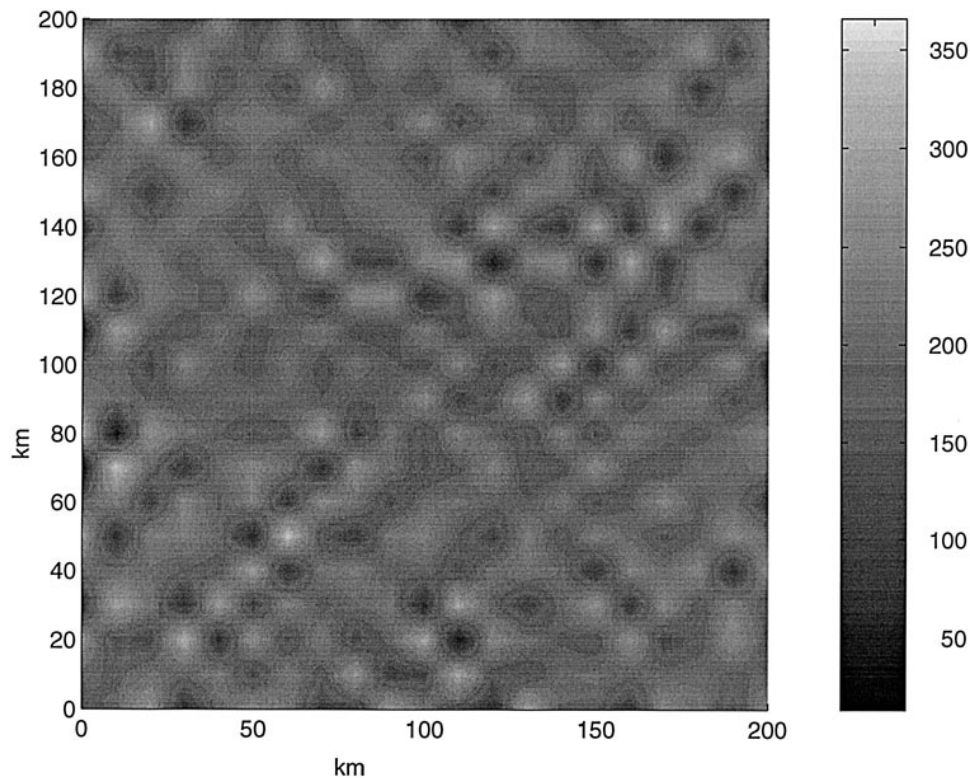


FIG. 2. Random field of surface sensible heat flux H_s at noontime with a banded white-noise spectral density function constant over the range of 20–50 km, and zero otherwise: $H_0 = 200 \text{ W m}^{-2}$ and $\sigma_H = 50 \text{ W m}^{-2}$.

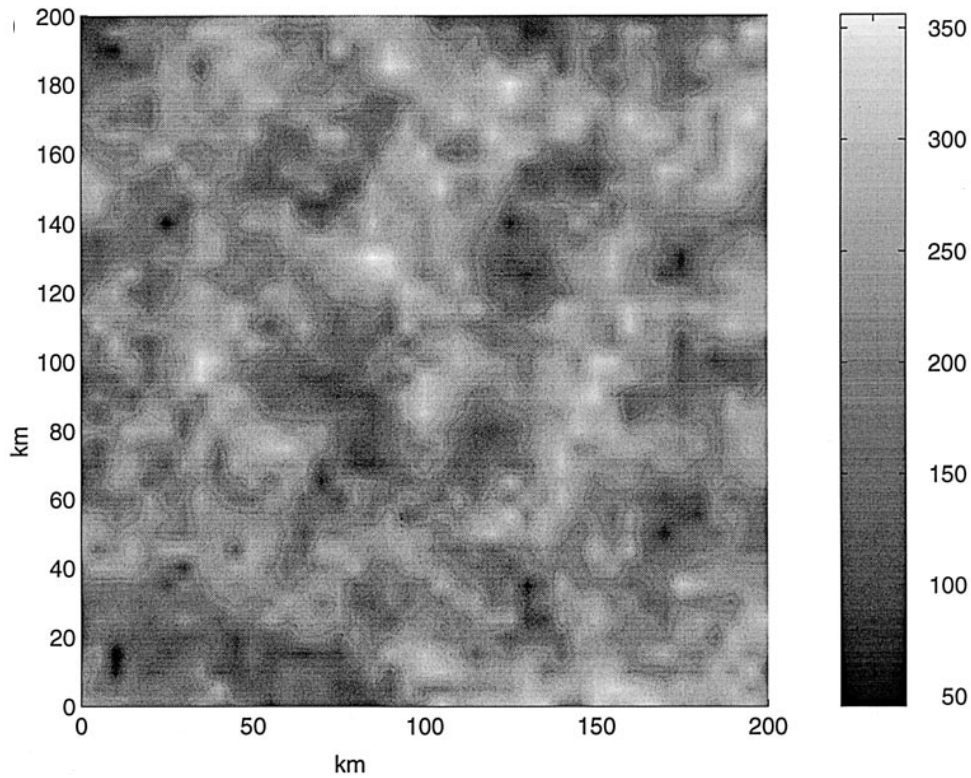


FIG. 3a. Random field of surface sensible heat flux H_s at noontime described by an exponential correlation function with correlation length $L = 10$ km, $H_0 = 200$ W m $^{-2}$, and $\sigma_H = 50$ W m $^{-2}$.

horizontal resolution should be small enough to represent the heterogeneity of the land surface and resolve the structure of the flow field. On the other hand, it should not be so small as to make the simulations too costly. Finite resolution imposes a limit on the finest scale of mesoscale circulation that can be resolved. Possible consequences of limited resolution will be discussed in section 5. Integration time step is 15 sec to ensure the stability of the numerical scheme. The total simulation time is 24 h, starting from sunrise.

a. Random distributions of surface heating

To realistically represent the observed heterogeneous land surface, we propose to model the TSHF $H_s(x, y; t)$ over the surface as a homogeneous random field. Realizations of this random field can be simulated by sampling from the spectrum and can be utilized as the input to the numerical CLARK model. The TSHF is prescribed in terms of

$$H_s(x, y; t) = \{H_0 + \sigma_H \hat{H}(x, y)\}I(t), \quad (1)$$

where H_0 is the domain-mean daily maximum turbulent sensible heat flux and σ_H is the corresponding standard deviation. The random function \hat{H} with zero mean and unit variance fully represents the spatial distribution of $H_s(x, y; t)$.

According to many observations, the time behavior of TSHF follows closely the insolation curve $I(t)$,

$$I(t) = \begin{cases} \sin\left(\frac{2\pi}{T_0}t\right), & 0 \leq t \leq T_0/2 \text{ (daytime)} \\ 0, & T_0/2 < t \leq T_0 \text{ (night)}, \end{cases} \quad (2)$$

where $t = 0$ refers to the time of sunrise and T_0 is the length of day.

Statistically \hat{H} may be characterized by a spectral density function or autocorrelation function (e.g., Yaglom 1987). Two types of hypothetical \hat{H} will be utilized in the numerical experiments: a banded white-noise spectral density function S_H and exponential correlation function R_H with correlation length of 10 km, 30 km, or 50 km. In practice they prove to be convenient approximations for many observed random processes (e.g., Wang 1997).

1) BANDED WHITE-NOISE SPECTRAL DENSITY FUNCTION

When the land surface heterogeneity lacks dominant length scales, the variability of the TSHF at the surface distributes uniformly over a wavenumber window. This type of random fields could be described by a banded white noise spectral density function. A low limit of 20

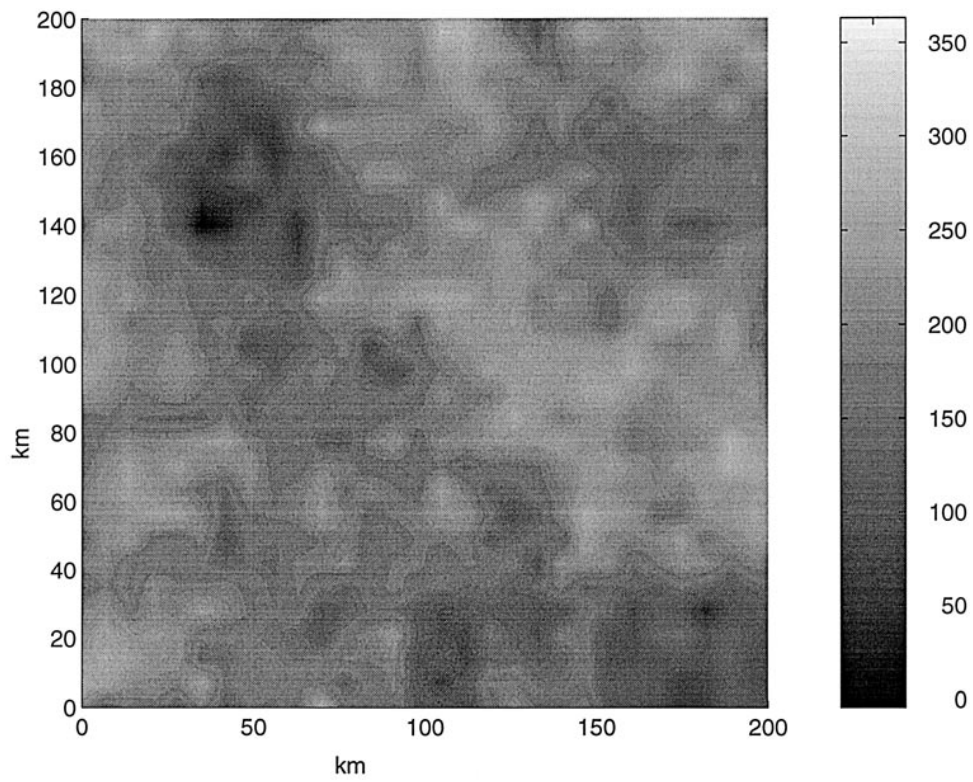


FIG. 3b. As in Fig. 3a but with correlation length $L = 30$ km.

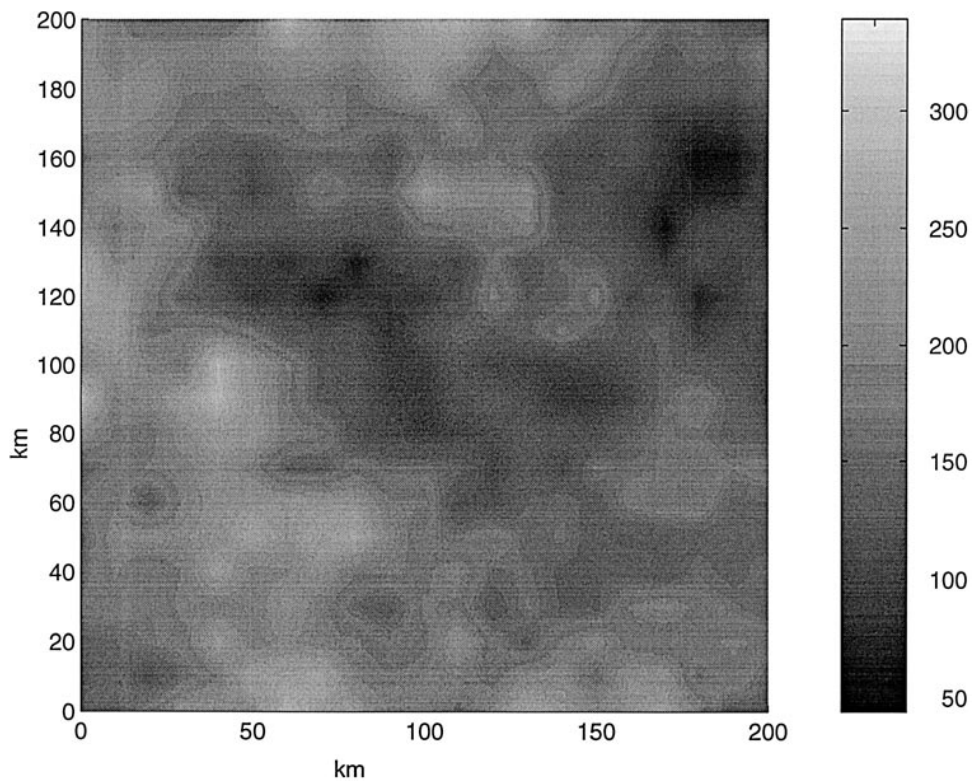


FIG. 3c. As in Fig. 3a but with a correlation length $L = 50$ km.

km and a high limit of 50 km are imposed on the length scale of the TSHF over the mesoscale simulation domain of 200 km in size. We may write the banded white noise spectral density function S_H as

$$S_H(k_1, k_2) = \begin{cases} \frac{1}{4(k_b - k_a)^2}, & k_a < |k_1|, |k_2| < k_b \\ 0, & \text{otherwise,} \end{cases} \quad (3)$$

where k_1, k_2, k_a and k_b are wavenumber with

$$k_a = \frac{2\pi}{50} \text{ km}^{-1}, \quad k_b = \frac{2\pi}{20} \text{ km}^{-1}.$$

A realization of the random field of H_s with S_H specified in (3) is illustrated in Fig. 2.

2) EXPONENTIAL AUTOCORRELATION FUNCTION

When the random field \hat{H} has a dominant length scale L , an exponential autocorrelation function R_H may be used to characterize it statistically,

$$R_H(x, y) = \exp\left(-\frac{\sqrt{x^2 + y^2}}{L}\right). \quad (4)$$

The spectral density function, or the Fourier transform of R_H , is (see appendix B for derivation)

$$S_H(k_1, k_2) = \frac{1}{2\pi L} \frac{1}{[L^{-2} + k^2]^{3/2}}, \quad (5)$$

where $k^2 = k_1^2 + k_2^2$.

The realizations of random field H_s , with spectrum S_H given in (5), with correlation length scales $L = 10, 30,$ and 50 km are plotted in Figs. 3a, 3b, and 3c, respectively.

Figures 2 and 3 assume H_0 to be 200 W m^{-2} and σ_H to be 50 W m^{-2} . These values lead to a range of the variability in H_s on the order of 200 W m^{-2} with a maximum H_s of $\sim 350 \text{ W m}^{-2}$ and a minimum H_s of $\sim 50 \text{ W m}^{-2}$. The basic features of these simulated random fields of TSHF H_s are reasonably close to the observations described in section 2.

b. Synoptic conditions

The parameters characterizing the synoptic environment in the numerical model for a dry atmosphere are time-invariant atmospheric stability N (Brunt–Väisälä frequency defined in appendix A) and uniform synoptic wind u_0 in time and space. Three vertical profiles of N are tested: neutral stratification ($N = 0$), stable stratification ($N = 10^{-2} \text{ s}^{-1}$), and neutral within the lowest 1-km layer and stable above. Three values of u_0 are used in simulations: 0, 5, and 10 m s^{-1} . The objective is to identify the condition(s) under which significant mesoscale circulation and fluxes may result.

c. Initial and boundary conditions

All simulations are initialized with no motion and start at sunrise. For example, $t = 9$ in the simulations means 1500 local solar time when the sunrise time is 0600. Cyclic lateral boundaries are used to mimic flow within an infinite domain. A free-slip surface is specified as the lower boundary condition. Absorbing layers are imposed at the top of the domain to simulate an unbounded atmosphere.

4. Results and discussions

Three variables are used to characterize the mesoscale circulation: mesoscale kinetic energy E_m , mesoscale momentum flux M_m , and mesoscale heat flux H_m . They are defined in terms of the variances of wind components, $\sigma_u^2, \sigma_v^2, \sigma_w^2$, and covariances between vertical velocity and the pertinent variables:

$$E_m(z, t) = \frac{1}{2}(\overline{\sigma_u^2} + \overline{\sigma_v^2} + \overline{\sigma_w^2}) \quad (6)$$

$$M_m(z, t) = \overline{w'u'} + \overline{w'v'} \quad (7)$$

$$H_m(z, t) = \overline{w'\theta'}, \quad (8)$$

where the primed terms stand for the perturbations around the (horizontal) domain means, and the average (represented by overbar) is carried out over the horizontal domain.

The numerical analysis will focus on evaluating the impact of the length scale of TSHF at the surface, atmospheric stability, and synoptic wind on the spatial-temporal distributions of $E_m, M_m,$ and H_m .

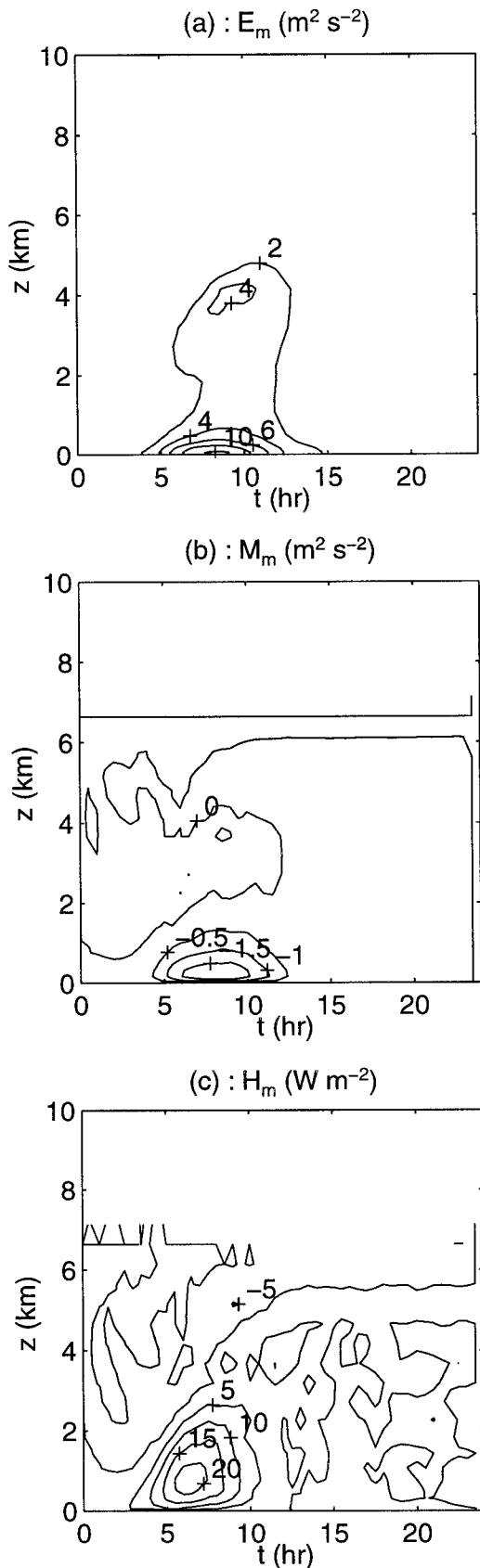
a. Effect of the length scale of the TSHF

1) BANDED WHITE-NOISE FORCING

The space-time distributions of $E_m, M_m,$ and H_m caused by the surface TSHF shown in Fig. 2 are plotted in Fig. 4. The maximum E_m , characterizing the intensity of the flow, is $10 \text{ m}^2 \text{ s}^{-2}$. A maximum horizontal wind of some 10 m s^{-1} and a maximum vertical velocity of about 3 m s^{-1} are stronger than a sea breeze circulation in this case. The diurnal variation of the mesoscale circulation peaks around 1500, consistent with the timing of sea breeze circulation. The circulation cells penetrate as high as 5 km, far beyond the depth of the observed planetary boundary layer (on the order of 1 km).

The associated vertical transport of horizontal momentum, represented by M_m , reaches a maximum value of $\sim 1.5 \text{ m}^2 \text{ s}^{-2}$ with the same timing as that of E_m . It is one order of magnitude greater than the turbulent momentum flux on the order of $0.05 \text{ m}^2 \text{ s}^{-2}$ (e.g., Stull 1988) in the boundary layer. But M_m is significant only up to ~ 2 km.

The vertical transport of heat, described by H_m , has a maximum of $\sim 20 \text{ W m}^{-2}$ at the ~ 1 km level and



decays moderately upward. A striking feature of H_m is that it has a different vertical profile from that of turbulent heat flux. This signature of H_m suggests that the mesoscale circulation could be the major heat transport mechanism in the free atmosphere where the turbulent heat flux is weak.

2) EXPONENTIAL AUTOCORRELATION FUNCTION FORCING

Distributions of $E_m(z, t)$, $M_m(z, t)$, and $H_m(z, t)$ corresponding to the surface TSHF shown in Figs. 3a–c are illustrated in Figs. 5a, 5b, and 5c, respectively. The E_m of $14 \text{ m}^2 \text{ s}^{-2}$ corresponds to a maximum horizontal wind of about 12 m s^{-1} and a maximum vertical wind about 2 m s^{-1} . The M_m of $\sim 1.4 \text{ m}^2 \text{ s}^{-2}$ is found to be downward and again much stronger than the corresponding turbulent flux. The maximum H_m of $\sim 20 \text{ W m}^{-2}$ is observed close to the $\sim 2 \text{ km}$ level, higher than that in the previous case. There are no significant differences in the magnitude and timing of E_m , M_m , and H_m for the exponential autocorrelation forcings with the three correlation length scales.

3) DISCUSSION

The random fields of TSHF shown in Figs. 2 and 3 differ visually and statistically as indicated by Eqs. (3) and (5). Particularly, the length scale of the TSHF shown in Fig. 2 is only up to 50 km, while that of Fig. 3 is not restricted. Nevertheless, they induce similar mesoscale circulation in terms of E_m , M_m , and H_m . This result implies that land surface heterogeneities with very large length scales are not important in forcing mesoscale circulations. On the other hand, the major variabilities in the TSHF for both types of correlation concentrate within a range of length scales on the order of tens of kilometers. Hence surface forcings with length scales around tens of kilometers are effective in driving mesoscale circulations.

The inherent length scale of the atmospheric system at mesoscales may be defined as the wavenumber (inversely proportional to the length scale) at which the amplitude of the *frequency response function* of the mesoscale circulation (see Wang et al. 1996) attains its maximum. Significant flow is expected to be induced when the length scales of the surface forcing are around the inherent length scale of the atmospheric system. As we discussed previously, the banded white-noise forcing with the length-scale (wavenumber) window of 20–50 km is as effective as the exponential correlation forcings

FIG. 4. Numerical simulation of mesoscale circulation under banded white noise forcing in an environment of $N = 0$ and $u_0 = 0$: (a) mesoscale kinetic energy E_m , (b) mesoscale momentum flux M_m , and (c) mesoscale heat flux H_m .

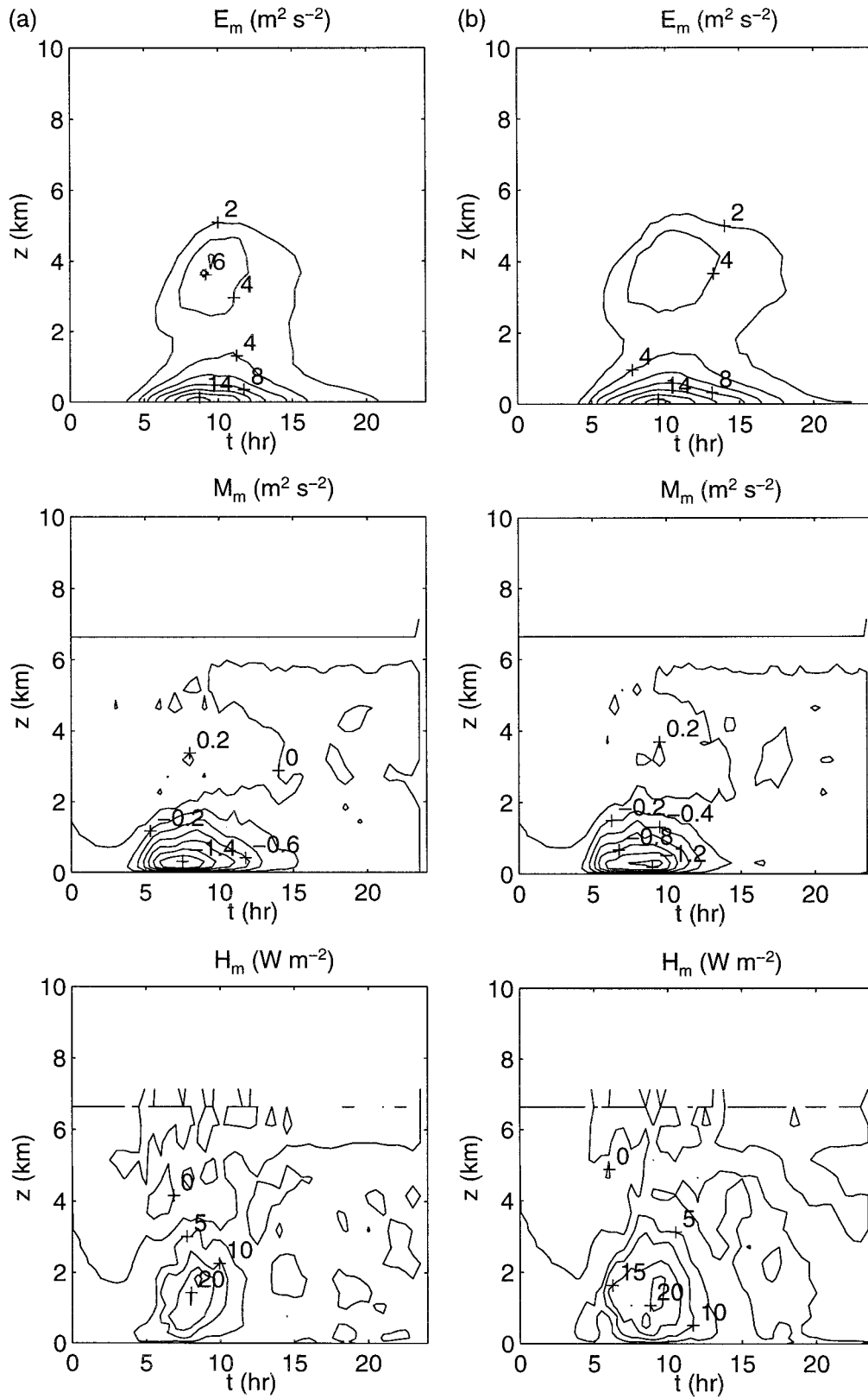


FIG. 5. Numerical simulation of mesoscale circulation under exponential autocorrelation forcing with (a) $L = 10$ km, (b) $L = 30$ km, and (c) $L = 50$ km in an environment of $N = 0$ and $u_0 = 0$.

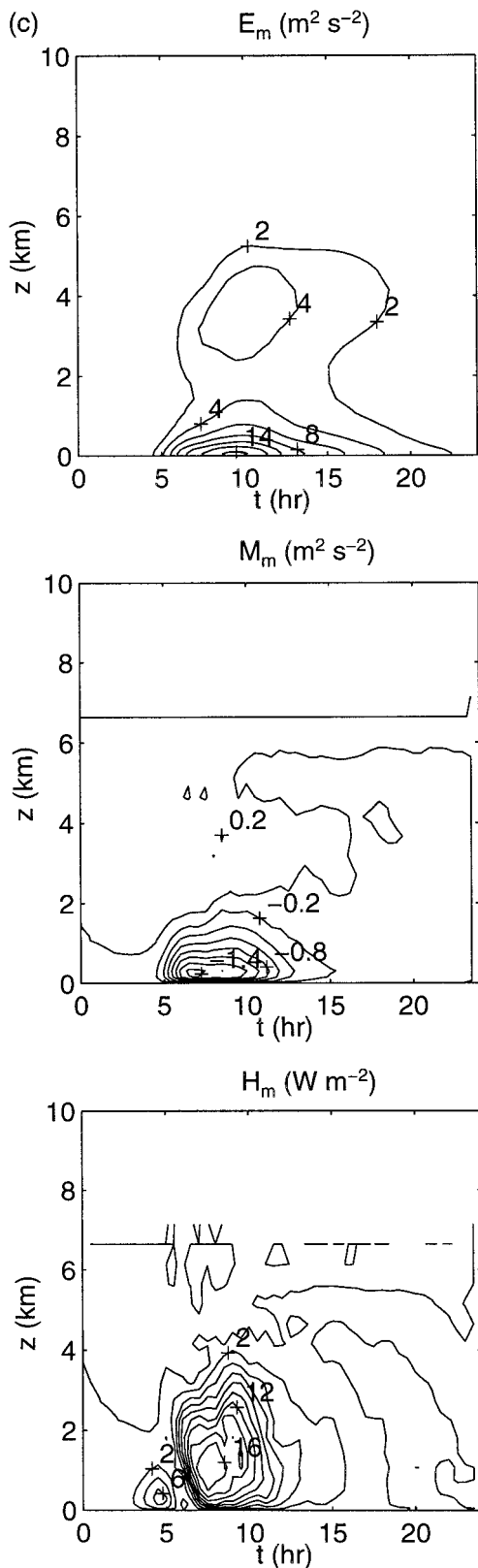


FIG. 5. (Continued)

with length-scale window of $0 - \infty$ km in driving mesoscale circulations. This finding suggests that the inherent length scale of mesoscale atmospheric system is likely to be around tens of kilometers.

b. Effect of atmospheric stability

1) CONSTANT N

Distributions of E_m , M_m , and H_m forced by the TSHF shown in Fig. 2 when the atmosphere is stable are presented in Fig. 6. The maximum E_m is about $0.5 \text{ m}^2 \text{ s}^{-2}$, only a few percent of the E_m shown in Fig. 4a where the atmosphere is neutral. The circulation cells are confined within the lowest few hundred meters layer. Here H_m becomes insignificant ($\sim 1.5 \text{ W m}^{-2}$). The maximum M_m of $\sim 0.06 \text{ m}^2 \text{ s}^{-2}$ is comparable to the turbulent flux. However, it occurs very close to the surface. Therefore, the mesoscale circulation in a stable atmosphere could be difficult to detect since it is likely to be masked by turbulence within the boundary layer.

2) VARYING N

Sometimes the stratification is nearly neutral within the depth of the boundary layer (~ 1 km) because of the mixing due to turbulent convection, and stable beyond the well-mixed layer. Here E_m , M_m , and H_m corresponding to this stability profile forced by the surface TSHF shown in Fig. 2 are presented in Fig. 7. As can be expected, the magnitudes of the three variables lie somewhere between those in the neutral and stable atmosphere. A maximum E_m of $4.5 \text{ m}^2 \text{ s}^{-2}$ corresponds to a maximum horizontal wind of 6 m s^{-1} and a maximum vertical wind of 1 m s^{-1} , comparable to the wind velocities of a sea breeze circulation. A maximum M_m of $\sim 0.6 \text{ m}^2 \text{ s}^{-2}$ is still significantly larger than the typical value of turbulent momentum flux. A maximum (downward) H_m of $\sim 10 \text{ W m}^{-2}$ is at ~ 500 m level, which is much lower than that in the neutral atmosphere. The penetration depth of the circulation cells is about 2 km. It is probably not easy to separate the signals of mesoscale circulation from that due to turbulence in this situation.

3) DISCUSSION

Atmospheric stability plays an important role in the development of mesoscale circulations. The presence of stable stratification strongly inhibits the free convection forced by random fields of TSHF in a dry atmosphere. It leads to relatively weak E_m and H_m that are likely to be masked by those due to turbulence within the boundary layer. However, M_m could still make an appreciable contribution to the total vertical transport of momentum.

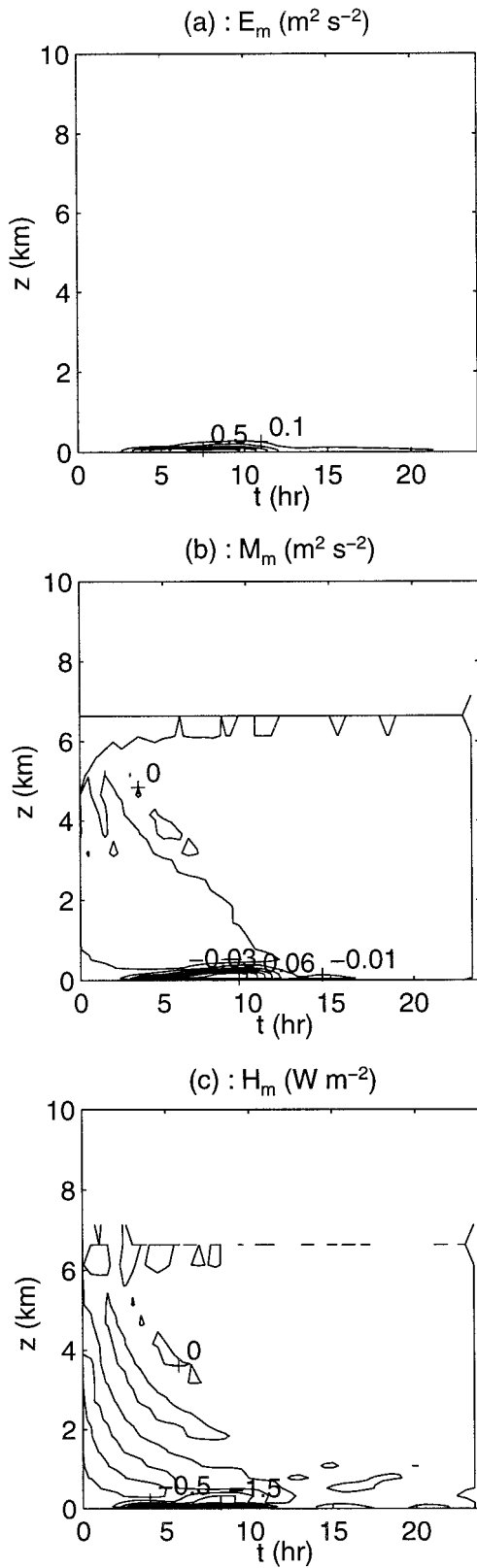


FIG. 6. Numerical simulation of mesoscale circulation under banded white noise forcing in a stable atmosphere $N = 10^{-2} \text{ s}^{-1}$ and zero synoptic wind $u_0 = 0$.

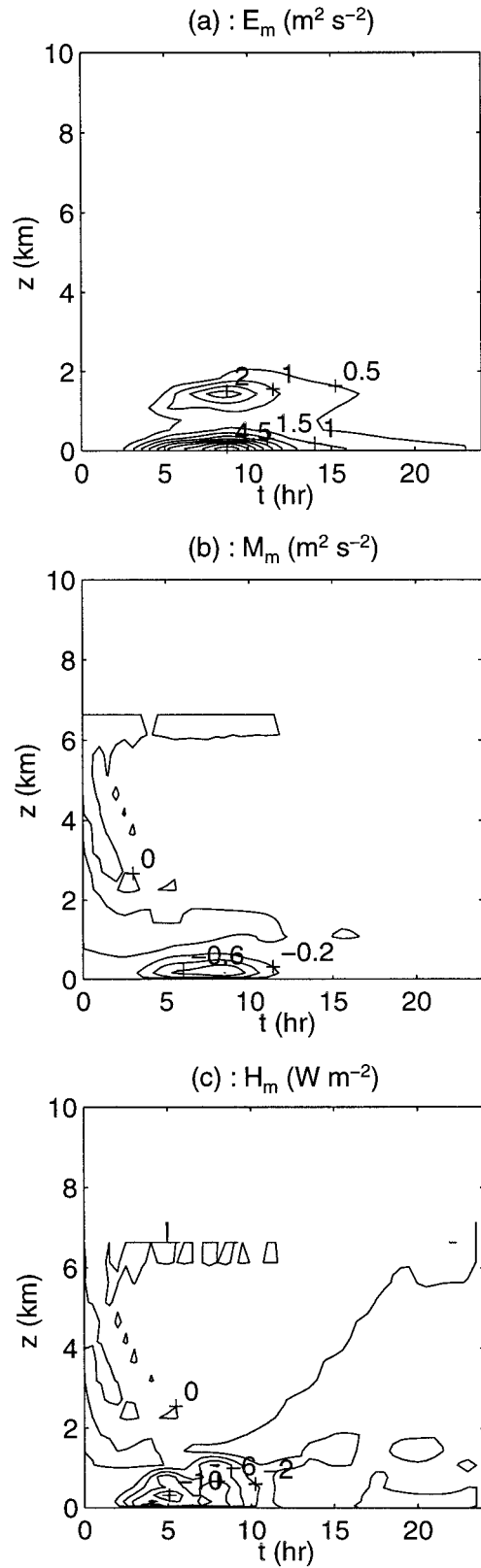


FIG. 7. As in Fig. 6 but in an atmosphere of varying stability ($N = 0$ in the lowest 1-km layer and $N = 10^{-2} \text{ s}^{-1}$ above) and zero synoptic wind $u_0 = 0$.

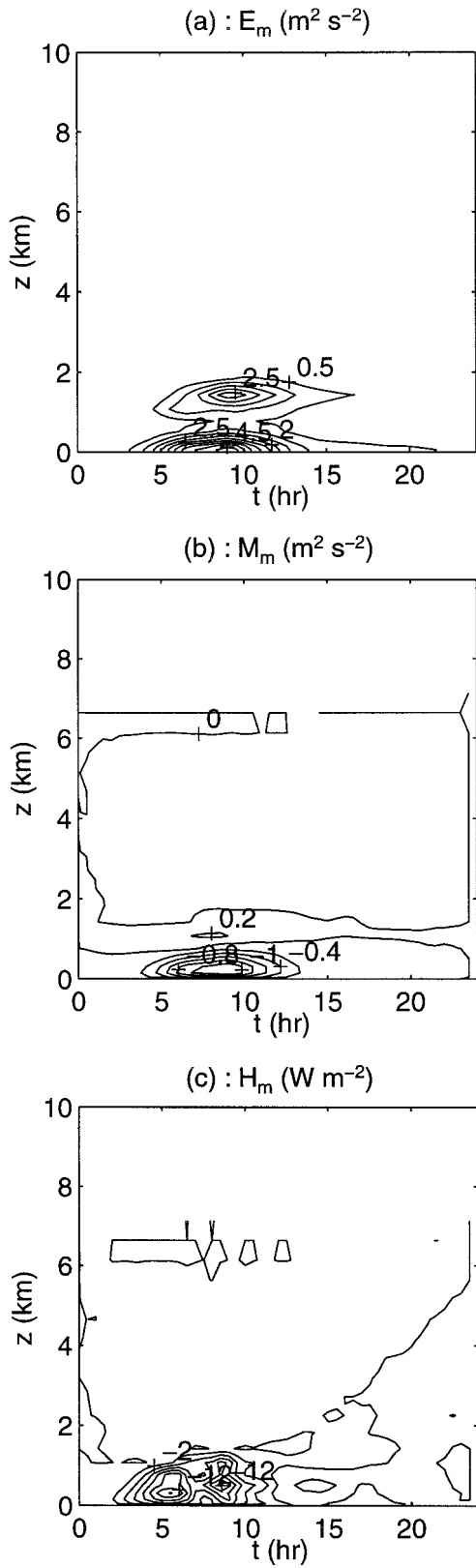


FIG. 8. As in Fig. 7 but for synoptic wind $u_0 = 5 m s^{-1}$.

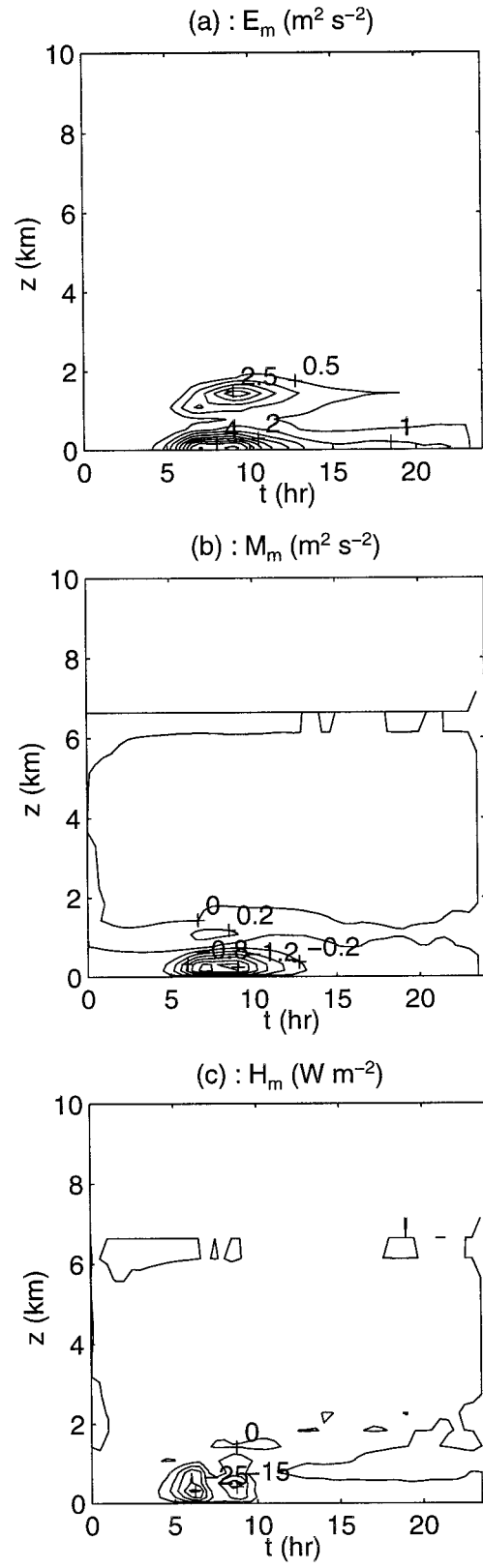


FIG. 9. As in Fig. 7 but for synoptic wind $u_0 = 10 m s^{-1}$.

c. Effect of synoptic wind

Figures 8 and 9 illustrate E_m , M_m , and H_m under the TSHF forcing shown in Fig. 2 when the synoptic winds are 5 and 10 m s⁻¹, respectively. A stratified atmosphere, with varying N , as in section 4b(2), is used. In general, synoptic winds up to 10 m s⁻¹ do not have strong effects on the results. When the synoptic winds increase from 0 to 10 m s⁻¹, no significant differences are found for E_m and M_m , while the maximum H_m increases from ~10 to ~25 W m⁻² with a delayed time of occurrence relative to the cases of zero synoptic wind. The inhibiting impact of synoptic wind on the mesoscale circulation predicted by the numerical model is much weaker than that based on the linear theory (Wang et al. 1996) under the same land surface conditions.

5. Comparison with the linear theory

The linear analysis of mesoscale circulation does not give identical results to those from the numerical simulations presented in this paper. Figure 10 shows E_m , M_m , and H_m predicted by the linear theory by Wang et al. (1996) under the random TSHF at the surface shown in Fig. 2. The corresponding results from the numerical simulations are shown in Fig. 4. The dissipation rate α in the linear theory was estimated (see appendix C) from the corresponding numerical simulation to make the comparison consistent.

Both similarities and discrepancies are apparent by comparing Fig. 10 with Fig. 4. The diurnal variation and vertical profile of E_m and H_m predicted by the linear theory are consistent with those from the numerical simulations. It indicates that the linear model is able to capture the basic physics behind the mesoscale circulation under the random surface forcing. On the other hand, the linear theory overestimates E_m and H_m relative to the numerical model by a factor of ~20. The linear theory does not produce M_m in the absence of synoptic wind.

The linear model differs from the nonlinear numerical model mainly in three aspects: nonlinear advection, dissipation process, and spatial resolution. The linear model ignores all nonlinear terms in the governing equations. Dissipation in the linear theory is represented in terms of Rayleigh friction with a constant coefficient. In the numerical model, dissipation is modeled in terms of velocity-dependent eddy diffusion. The numerical model also suffers from a restriction on spatial resolution that limits the resolved structure of mesoscale circulations. These three factors are believed to be mainly responsible for the discrepancies between the results from the linear analytical model and the nonlinear numerical model.

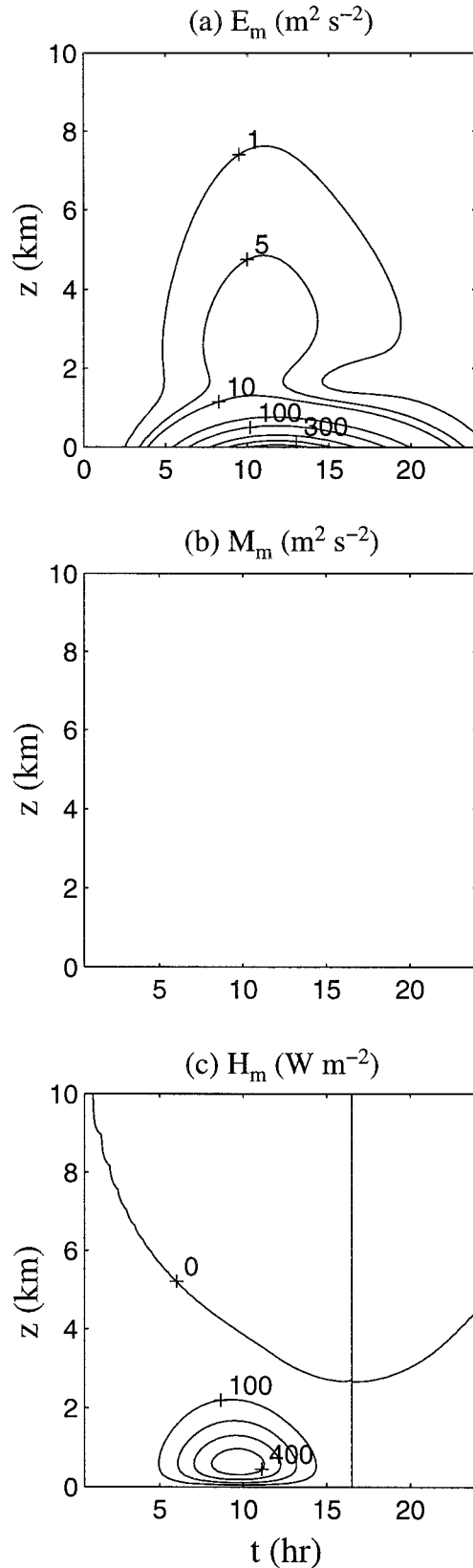


FIG. 10. Stochastic linear theory of mesoscale circulation under banded white noise forcing in an atmosphere of neutral stratification ($N = 0$) and zero synoptic wind ($u_0 = 0$).

a. Nonlinear advection

The nonlinear terms represent the transport of momentum associated with the flow. Linearization implies that there is no momentum transport mechanism when the synoptic wind is zero. That is not the case with the numerical model. The underestimation of momentum flux and the sensitivity of the flow to stability and synoptic wind predicted by the linear theory relative to the numerical model are, to a large extent, attributed to the omission of nonlinear advection terms. This argument is further supported by the fact that assuming zero eddy diffusion coefficient in the numerical model does not eliminate momentum flux. Hence the existence of momentum flux in the absence of synoptic wind is not caused by dissipation. A complete treatment of nonlinear advection terms awaits the development of a nonlinear analytical model.

b. Dissipation process

Dissipation is an important factor in determining the timing and magnitude of mesoscale circulation. The linear theory produces a maximum E_m of $60 \text{ m}^2 \text{ s}^{-2}$ at 1600 [inferred from Fig. 2 of Wang et al. (1996)] and a maximum H_m of 150 W m^{-2} at 1500 (Fig. 9b of the same paper) local solar time for the dissipation parameter $\alpha = 1.2\Omega_0$. Figure 10a shows it produces a maximum E_m of $300 \text{ m}^2 \text{ s}^{-2}$ at 1800 and a maximum H_m of 400 W m^{-2} at 1500 for $\alpha = 0.6\Omega_0$ (see appendix C) under the same surface forcing and synoptic conditions. The numerical simulation (Fig. 4a) produces a maximum of E_m of $10 \text{ m}^2 \text{ s}^{-2}$ at 1500 and a maximum H_m of 20 W m^{-2} at 1300. Greater dissipation coefficient α is needed for the linear model to reproduce the timing and magnitude of the E_m and H_m predicted by the numerical simulation.

c. Spatial resolution

The resolved structure of the mesoscale circulation in the numerical simulation is limited by the spatial resolution of the numerical model. The wind velocity, temperature, and pressure computed at the grid points should be regarded as the averaged values over the grid area. The subgrid variabilities of the mesoscale circulation, if any, are smoothed out by the discretization of the governing equations. Hence, in principle, numerical simulation tends to underestimate E_m , M_m , and H_m relative to the true values by ignoring the subgrid variability of the flow field due to the limited spatial resolution of numerical model.

Exact distribution of the variability of the nonlinear flow over the entire wavenumber range is not known. As an alternative, the analytical solution derived in Wang et al. (1996) may help to demonstrate the effect of subgrid smoothing of the flow field on the values of E_m , M_m , and H_m . The reduction factor due to subgrid smoothing depends on the grid size Δ and wavenumber k_1 , k_2 in the following way (see appendix D):

$$\left[\frac{\sin\left(k_1 \frac{\Delta}{2}\right)}{k_1 \frac{\Delta}{2}} \right]^2 \left[\frac{\sin\left(k_2 \frac{\Delta}{2}\right)}{k_2 \frac{\Delta}{2}} \right]^2. \quad (9)$$

Once the grid size Δ is chosen, (9) shows that variability in the flow field at length scales below Δ is filtered out, leading to an underestimation of E_m , M_m , and H_m .

Figure 11 shows that E_m , M_m , and H_m predicted by the linear theory are reduced by a factor of ~ 2 when the spatial resolution of the linear model is around 10 km. So spatial resolution is expected to have a significant effect on the numerical simulation of mesoscale circulation. As discussed earlier, the numerical model produces E_m , M_m , and H_m that are tens of times smaller than the corresponding values from linear analysis. It is unlikely that finite resolution alone is responsible completely for the differences between the linear and nonlinear models.

6. Conclusions

Several conclusions may be drawn from the numerical model simulations that have been described in this paper.

- Atmospheric stability is an important factor in the development of mesoscale circulations. The circulation cells could reach 5-km height in an atmosphere with neutral stratification but are suppressed down to a layer not more than 200 m in depth near the surface in a stable atmosphere. When the near-surface layer is neutral and the atmosphere above is stable, the mesoscale circulation is confined within a layer of 2 km in depth. We argue that the stable stratification provides the dominant resistance to the atmosphere against the TSHF forcing of random distribution. Stability strongly inhibits the development of mesoscale circulation and mesoscale fluxes.
- The effects of the synoptic wind are relatively weak compared to that of the stability. The presence of moderate synoptic wind increases slightly the mesoscale circulation and fluxes, in contrast to the inhibiting role of synoptic wind predicted by the linear theory. A possible negative feedback between the mesoscale and the large-scale circulations is implied since enhancement of mesoscale momentum fluxes (downward) in turn leads to a stronger resistance to the large-scale circulation.
- Any random distribution of TSHF at the surface with dominant length scales around a few tens of kilometers will be equally effective in driving mesoscale circulations. Land surface heterogeneity with very large length scales is not important in mesoscale circulations. The functional form of the spectrum or correlation function of the surface forcing is not critical.
- Mesoscale momentum flux is one order of magnitude

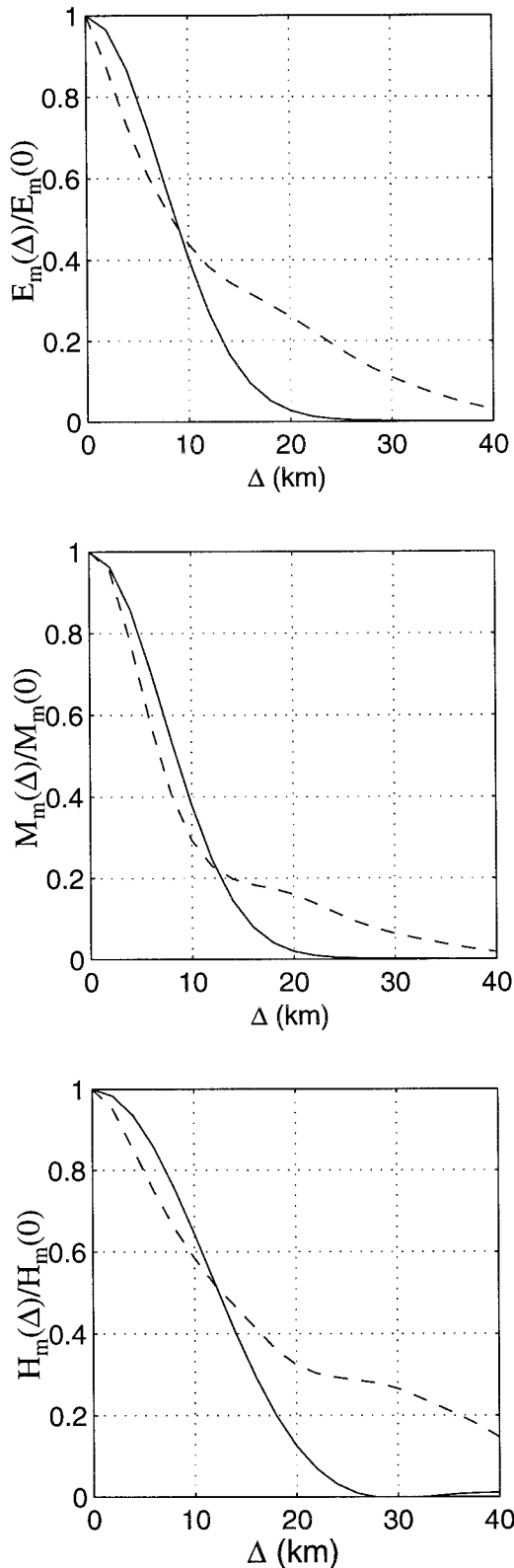


FIG. 11. Normalized E_m , M_m , and H_m as function of grid size Δ under banded white-noise forcing (solid line), and exponential correlation with length scale of 30-km forcing (broken line) in an environment of $N = 0$ and $u_0 = 0.4 \text{ m s}^{-1}$ at $t = 9 \text{ h}$.

stronger than the corresponding turbulent flux in a neutral or a neutral-stable atmosphere. In a stable atmosphere, mesoscale and turbulent momentum fluxes are still comparable. Hence mesoscale circulation is effective in the vertical transport of kinetic energy.

- Mesoscale circulations provide a dominant heat transport mechanism beyond a certain level (on the order of 1 km and up). Mesoscale heat flux has a different vertical distribution from the turbulent heat flux. The maximum mesoscale heat flux of $\sim 20 \text{ W m}^{-2}$ (upward) occurs at a level close to 2 km in a neutral atmosphere where turbulent heat flux is usually weak. Stable stratification tends to reverse the direction of mesoscale heat flux. A mixed neutral-stable stability profile reduces this level down to $\sim 300 \text{ m}$. Mesoscale heat flux is probably insignificant in a stable atmosphere.
- The discrepancies between the numerical simulation and the linear analysis are caused collectively by three factors: nonlinear advection terms, dissipation, and spatial resolution. A grid size of 10 km in the numerical model could result in a reduction in kinetic energy, momentum, and heat flux by a factor of ~ 2 due to subgrid smoothing. A dissipation coefficient greater than that estimated from the nonlinear numerical model is required for the linear theory to reproduce the same magnitude and timing of the mesoscale circulation as the numerical simulation.
- Nonlinear advection terms are responsible for the mesoscale momentum fluxes. It has been found from the simulations that momentum fluxes may result regardless of the turbulent dissipation in the numerical model. So satisfactory prediction of the vertical transport of kinetic energy induced by land surface heterogeneity requires nonlinear modeling of mesoscale circulations.

These results are potentially useful in the subgrid parameterization of large-scale models, particularly when the subgrid land surface heterogeneity has complex distribution that can be described by a homogeneous random field. One basic feature of the mesoscale circulation is that mesoscale kinetic energy, momentum flux, and heat flux vary in time and height in a way very different from the corresponding turbulent ones. To assess the additional contribution to the total transport of energy by subgrid mesoscale processes, three parameters have been identified to be important: standard deviation and length scale(s) of the TSHF over the land surface, and the atmospheric stability. The homogeneous random field description of land surface heterogeneity is a powerful tool in handling the complexity in the surface forcing for mesoscale circulations. We realize that the statistical homogeneity assumption may impose a restriction on the validity and accuracy of some our conclusions. This work should be regarded as a complement to many previous efforts dealing with land surface forcing following regular patterns.

Another related issue is the possible triggering of moist convection by the mesoscale circulation, which may lead to rainfall formation. Some of our ongoing research focuses on this topic and will be reported in the future.

Acknowledgments. This work was supported by the National Science Foundation under Grants EAR-9120386 and ATM-9020832. The views, opinions, and/or findings contained in this report are those of the authors and should not be considered as an official position of the National Science Foundation.

The simulations were carried out on a CRAY Y-MP8/864 machine at NCAR. We gratefully acknowledge the National Center for Atmospheric Research, which is sponsored by the National Science Foundation, for the computing time used in this research. Special thanks go to CLARK modelers, particularly to Ms. Janice Coen for her invaluable advice and constant assistance through out this work. We are grateful to Dr. Jeff Eidenshink, who generously provided the software for processing the NDVI data.

APPENDIX A

List of Symbols

E_m	mesoscale kinetic energy
H_m	mesoscale heat flux
M_m	mesoscale momentum flux
H_s	turbulent sensible heat flux at surface
k	radius wavenumber $(k_1^2 + k_2^2)^{1/2}$
k_1, k_2	wavenumber in x and y directions
L	length scale
N	constant Brunt-Väisälä frequency defined as $\sqrt{(g/\theta_0)(\partial\theta/\partial z)}$
$S(k_1, k_2)$	spectral density function
r	radius distance $\sqrt{x^2 + y^2}$
t	time
T_0	length of a day (24 h)
u, v, w	wind velocity in $x, y,$ and z directions
u_0	constant synoptic wind in x direction
x, y	horizontal coordinates
z	vertical coordinate
α	coefficient of Rayleigh friction
$\bar{\theta}$	large-scale background potential temperature
θ_0	constant reference potential temperature
σ^2	variance
Ω_0	rotation rate of the earth ($=2\pi/T_0$)

APPENDIX B

Derivation of Eq. (5)

The Wiener-Khinchine theorem (e.g., Yaglom 1987) states that the correlation function $R_H(x, y)$ and spectral density function $S_H(k_1, k_2)$ of a homogeneous random

function H in the (x, y) domain constitute a Fourier transform pair; that is,

$$S_H(k_1, k_2) = \frac{1}{4\pi^2} \int_{-\infty}^{\infty} \int_{-\infty}^{\infty} R_H(x, y) e^{-i(k_1x + k_2y)} dx dy. \quad (\text{B1})$$

When $R_H(x, y)$ has the functional form given in Eq. (4), we have (e.g., Bras and Rodríguez-Iturbe 1985)

$$\begin{aligned} S_H(k_1, k_2) &= \frac{1}{4\pi^2} \int_{-\infty}^{\infty} \int_{-\infty}^{\infty} e^{-\sqrt{x^2 + y^2}/L} e^{-i(k_1x + k_2y)} dx dy \\ &= \frac{1}{2\pi} \int_0^{\infty} e^{-(r/L)} \left\{ \frac{1}{2\pi} \int_0^{2\pi} \cos(kr \cos\theta) d\theta \right\} r dr \\ &= \frac{1}{2\pi} \int_0^{\infty} e^{-(r/L)} J_0(kr) r dr, \end{aligned} \quad (\text{B2})$$

where $J_0(x)$ is the zeroth-order Bessel function of the first kind. The integral on the right of Eq. (B2), from Gradshtein and Ryzhik (1994), is

$$S_H(k_1, k_2) = \frac{1}{2\pi L} [L^{-2} + k^2]^{-3/2}.$$

APPENDIX C

Estimation of Dissipation Rate α

The linear theory parameterizes the momentum and heat dissipation by Rayleigh friction with a constant parameter α . The dissipation in the numerical CLARK model is represented by eddy diffusion. Hence, α needs to be determined in order to make consistent evaluation of the linear theory against the numerical simulation. The time-varying potential temperature obtained from the numerical simulation can be used to estimate the value of α .

Equation (3) for buoyancy b , a linear function of potential temperature θ , in the stochastic linear theory (Wang et al. 1996) is

$$\frac{\partial b}{\partial t} + u_0 \frac{\partial b}{\partial x} + N^2 w = Q(x, y, z, t) - \alpha b, \quad (\text{C1})$$

which reduces to a simpler form for neutral atmosphere ($N = 0$), zero synoptic wind ($u_0 = 0$), and nighttime ($Q = 0$),

$$\frac{\partial b}{\partial t} = -\alpha b. \quad (\text{C2})$$

Equation (C2) implies that the standard deviation of potential temperature θ , σ_θ , satisfies the following equation,

$$\frac{\partial \sigma_\theta}{\partial t} = -\alpha \sigma_\theta. \quad (\text{C3})$$

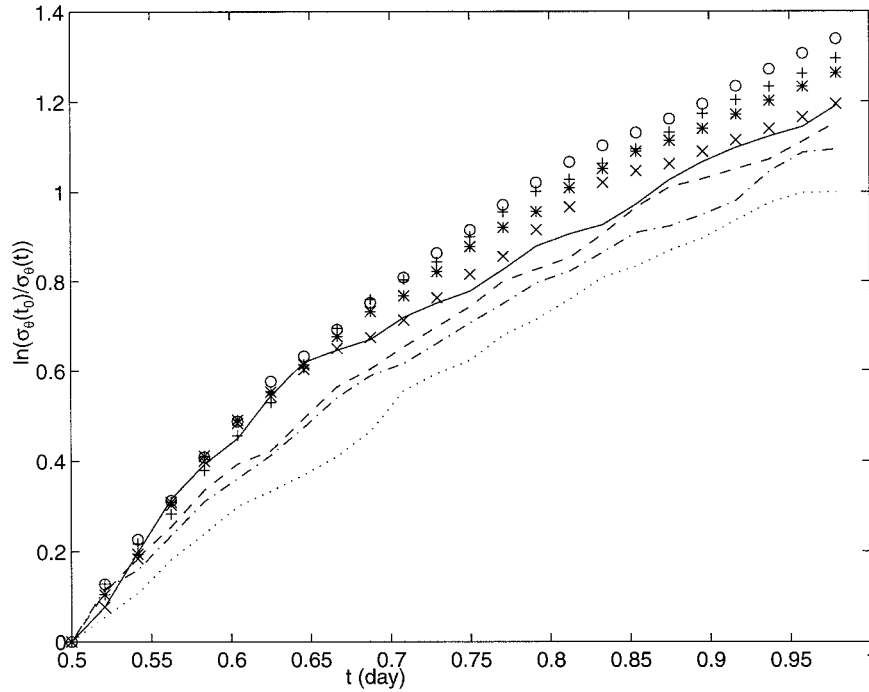


FIG. C1. Standard deviation of potential temperature σ_θ vs time t at $z = 53$ m (+); $z = 156$ m (o); $z = 306$ m (*); $z = 513$ m (x); $z = 768$ m (solid); $z = 1073$ m (dash); $z = 1428$ m (dash-dot); $z = 1826$ m (dot) obtained from the simulation of Fig. 4.

Constant α can be derived from the solution of σ_θ according to Eq. (C3):

$$\alpha = \frac{1}{t - t_0} \ln \frac{\sigma_\theta(z, t_0)}{\sigma_\theta(z, t)}, \quad (C4)$$

where t_0 is the time of sunset or 1800 local solar time.

Figure C1 shows the σ_θ versus t obtained from the simulation of Fig. 4 at different vertical levels. The value of α based on Fig. C1 ranges from 2 day^{-1} to 4 day^{-1} . This is equivalent to

$$\alpha = (0.32 \sim 0.64) \frac{2\pi}{T_0} = (0.32 \sim 0.64) \Omega_0. \quad (C5)$$

The value of α does not sensitively depend on the distribution of the land surface heating.

Figure 10 shows E_m , M_m , and H_m produced by the linear theory where α is $0.6\Omega_0$.

APPENDIX D

E_m , M_m , and H_m Computed Using the Horizontally Smoothed Flow Field

Denote a grid-averaged dependent variable ξ by $\tilde{\xi}$,

$$\tilde{\xi}(x, y, z, t) = \frac{1}{\Delta^2} \int_{x-(\Delta/2)}^{x+(\Delta/2)} \int_{y-(\Delta/2)}^{y+(\Delta/2)} \xi(\tilde{x}, \tilde{y}, z, t) d\tilde{x}d\tilde{y}. \quad (D1)$$

Assuming horizontal homogeneity in ξ allows the use of spectral representation for ξ ,

$$\xi = \int_{-\infty}^{\infty} \int_{-\infty}^{\infty} e^{i(k_1x+k_2y)} dZ_\xi(k_1, k_2; z, t). \quad (D2)$$

Substituting (D2) into (D1) leads to

$$\begin{aligned} \tilde{\xi} &= \frac{1}{\Delta^2} \int_{x-(\Delta/2)}^{x+(\Delta/2)} \int_{y-(\Delta/2)}^{y+(\Delta/2)} \int_{-\infty}^{\infty} \int_{-\infty}^{\infty} e^{i(k_1\tilde{x}+k_2\tilde{y})} dZ_\xi(k_1, k_2; z, t) d\tilde{x}d\tilde{y} \\ &= \int_{-\infty}^{\infty} \int_{-\infty}^{\infty} \left\{ \frac{1}{\Delta^2} \int_{x-(\Delta/2)}^{x+(\Delta/2)} \int_{y-(\Delta/2)}^{y+(\Delta/2)} e^{i(k_1\tilde{x}+k_2\tilde{y})} d\tilde{x}d\tilde{y} \right\} dZ_\xi(k_1, k_2; z, t), \end{aligned} \quad (D3)$$

where

$$\frac{1}{\Delta} \int_{x-(\Delta/2)}^{x+(\Delta/2)} e^{ik_1\bar{x}} d\bar{x} = e^{ik_1x} \frac{\sin\left(k_1 \frac{\Delta}{2}\right)}{k_1 \frac{\Delta}{2}}$$

$$\frac{1}{\Delta} \int_{y-(\Delta/2)}^{y+(\Delta/2)} e^{ik_2\bar{y}} d\bar{y} = e^{ik_2y} \frac{\sin\left(k_2 \frac{\Delta}{2}\right)}{k_2 \frac{\Delta}{2}}.$$

Therefore, $\tilde{\xi}$ is a horizontally homogeneous random field with the spectral representation

$$\tilde{\xi}(x, y, z, t) = \int_{-\infty}^{\infty} \int_{-\infty}^{\infty} e^{i(k_1x+k_2y)} \left[\frac{\sin\left(k_1 \frac{\Delta}{2}\right)}{k_1 \frac{\Delta}{2}} \left| \frac{\sin\left(k_2 \frac{\Delta}{2}\right)}{k_2 \frac{\Delta}{2}} \right| \right] dZ_{\xi}(k_1, k_2; z, t). \quad (\text{D4})$$

The mesoscale kinetic energy \tilde{E}_m , momentum flux \tilde{M}_m , and heat flux \tilde{H}_m using the smoothed variables can be written as function of grid size Δ , according to Wang et al. (1996),

$$\tilde{E}_m(\Delta) = \int_{-\infty}^{\infty} \int_{-\infty}^{\infty} \left[\frac{\sin\left(k_1 \frac{\Delta}{2}\right)}{k_1 \frac{\Delta}{2}} \right]^2 \left[\frac{\sin\left(k_2 \frac{\Delta}{2}\right)}{k_2 \frac{\Delta}{2}} \right]^2 (|\Pi_u|^2 + |\Pi_v|^2 + |\Pi_w|^2) \sigma_Q^2 S_Q dk_1 dk_2 \quad (\text{D5})$$

$$\tilde{M}_m(\Delta) = \int_{-\infty}^{\infty} \int_{-\infty}^{\infty} \left[\frac{\sin\left(k_1 \frac{\Delta}{2}\right)}{k_1 \frac{\Delta}{2}} \right]^2 \left[\frac{\sin\left(k_2 \frac{\Delta}{2}\right)}{k_2 \frac{\Delta}{2}} \right]^2 |\Pi_u \Pi_w + \Pi_v \Pi_w| \sigma_Q^2 S_Q dk_1 dk_2 \quad (\text{D6})$$

$$\tilde{H}_m(\Delta) = \int_{-\infty}^{\infty} \int_{-\infty}^{\infty} \left[\frac{\sin\left(k_1 \frac{\Delta}{2}\right)}{k_1 \frac{\Delta}{2}} \right]^2 \left[\frac{\sin\left(k_2 \frac{\Delta}{2}\right)}{k_2 \frac{\Delta}{2}} \right]^2 |\Pi_{\theta} \Pi_w| \sigma_Q^2 S_Q dk_1 dk_2, \quad (\text{D7})$$

where Π functions are the frequency response functions, Q is the buoyancy source at surface, and σ_Q is the standard deviation of Q defined in Wang et al. (1996).

Figure 11 demonstrates \tilde{E}_m , \tilde{M}_m , and \tilde{H}_m varying with Δ under banded white noise forcing (column a) and exponential correlation with correlation length of 30-km forcing (column b), respectively. The curves are computed at $t = 9$ h when the mesoscale circulation reaches maximum. The synoptic environment is char-

acterized by neutral stability and slight large-scale wind of 0.4 m s^{-1} in order to get nonzero momentum flux.

REFERENCES

- André, J.-C., P. Bougeault, and J.-P. Goutorbe, 1990: Regional estimates of heat and evaporation fluxes over nonhomogeneous terrain: Examples from the HAPEX-MOBILHY Programme. *Bound.-Layer Meteor.*, **50**, 77–108.

- Avissar, R., and R. A. Pielke, 1989: A parameterization of heterogeneous land-surface for atmospheric numerical models and its impact on regional meteorology. *Mon. Wea. Rev.*, **117**, 2113–2136.
- , and F. Chen, 1993: Development and analysis of prognostic equations for mesoscale kinetic energy and mesoscale (subgrid scale) fluxes for large-scale atmospheric models. *J. Atmos. Sci.*, **50**, 3751–3774.
- Bras, R. L., and I. Rodríguez-Iturbe, 1985: *Random Function and Hydrology*. Addison-Wesley, 559 pp.
- Clark, T. L., 1977: A small-scale dynamic model using a terrain-following coordinate transformation. *J. Comput. Phys.*, **24**, 186–215.
- Dalu, G. A., and R. A. Pielke, 1989: An analytical study of the sea breeze. *J. Atmos. Sci.*, **46**, 1815–1825.
- , and —, 1993: Vertical heat fluxes generated by mesoscale atmospheric flow induced by thermal inhomogeneities in the PBL. *J. Atmos. Sci.*, **50**, 919–926.
- Desjardins, R. L., P. H. Schuepp, J. I. MacPherson, and D. J. Buckley, 1992: Land surface measurements from the split window channels of the NOAA 7 Advanced Very High Resolution Radiometer. *J. Geophys. Res.*, **97**, 18 467–18 475.
- Doran, J. C., W. J. Shaw, and J. M. Hubbe, 1995: Boundary layer characteristics over areas of inhomogeneous surface fluxes. *J. Appl. Meteor.*, **34**, 559–571.
- Eidenshink, J. C., 1992: The 1990 conterminous U.S. AVHRR data set. *Photogramm. Eng. Remote Sens.*, **58**, 809–813.
- Gradshtein, I. S., and I. M. Ryzhik, 1994: *Tables of Integrals, Series, and Products*. Academic Press, 1204 pp.
- Huss, A., and Y. Feliks, 1981: A mesometeorological numerical model of the sea and land breeze involving sea-atmospheric interactions. *Contrib. Atmos. Phys.*, **54**, 238–257.
- Li, B., and R. Avissar, 1994: The impact of spatial variability of land-surface characteristics on land-surface heat fluxes. *J. Climate*, **7**, 527–537.
- Lynn, B. H., F. Abramopoulos, and R. Avissar, 1995a: Using similarity theory to parameterize mesoscale heat fluxes generated by subgrid-scale landscape discontinuities in GCMs. *J. Climate*, **8**, 932–951.
- , D. Rind, and R. Avissar, 1995b: The importance of mesoscale circulations generated by subgrid-scale landscape heterogeneities in general circulation models. *J. Climate*, **8**, 191–205.
- Mahfouf, J.-F., E. Richard, and P. Mascart, 1987: The influence of soil and vegetation on the development of mesoscale circulations. *J. Climate Appl. Meteor.*, **26**, 1483–1495.
- Mahrer, Y., and R. A. Pielke, 1977: A numerical study of the airflow over irregular terrain. *Contrib. Atmos. Phys.*, **50**, 98–113.
- Mahrt, L., and M. Ek, 1993: Spatial variability of turbulent fluxes and roughness lengths in HAPEX-MOBILHY. *Bound.-Layer Meteor.*, **65**, 381–400.
- Ookouchi, Y., M. Segal, R. C. Kessler, and R. A. Pielke, 1984: Evaluation of soil moisture effects on the generation and modification of mesoscale circulations. *Mon. Wea. Rev.*, **112**, 2281–2292.
- Pielke, R. A., 1974: A three-dimensional numerical model of sea breeze over south Florida. *Mon. Wea. Rev.*, **102**, 115–139.
- , 1984: *Mesoscale Meteorological Modeling*. Academic Press, 612 pp.
- , G. A. Dalu, J. S. Snook, T. J. Lee, and T. G. F. Kittel, 1991: Nonlinear influence of mesoscale land use on weather and climate. *J. Climate*, **4**, 1053–1069.
- Rotunno, R., 1983: On the linear theory of the land sea breeze. *J. Atmos. Sci.*, **40**, 1999–2009.
- Segal, M., J. F. W. Purdom, J. L. Song, R. A. Pielke, and Y. Mahrer, 1986: Evaluation of cloud shading effects on the generation and modification of mesoscale circulations. *Mon. Wea. Rev.*, **114**, 1201–1212.
- , R. Avissar, M. C. McCumber, and R. A. Pielke, 1988: Evaluation of vegetation effects on the generation and modification of mesoscale circulations. *J. Atmos. Sci.*, **45**, 2268–2286.
- , W. E. Schreiber, G. Kallos, J. R. Garratt, A. Rodi, J. Weaver, and R. A. Pielke, 1989: The impact of crop areas in northern Colorado on midsummer mesoscale thermal circulations. *Mon. Wea. Rev.*, **117**, 809–825.
- Stull, R. B., 1988: *An Introduction to Boundary Layer Meteorology*. Kluwer Academic, 666 pp.
- Sun, J., and L. Mahrer, 1994: Spatial distribution of surface fluxes estimated from remotely sensed variables. *J. Appl. Meteor.*, **33**, 1341–1353.
- Wang, J., 1997: A study of mesoscale circulation induced by land surface heterogeneity. Ph.D. dissertation, Massachusetts Institute of Technology, 164 pp.
- , R. Bras, and E. A. B. Eltahir, 1996: A stochastic linear theory of mesoscale circulation induced by the thermal heterogeneity of the land surface. *J. Atmos. Sci.*, **53**, 3349–3366.
- Xian, Z., and R. A. Pielke, 1991: The effects of width of landmasses on the development of sea breezes. *J. Appl. Meteor.*, **30**, 1280–1304.
- Yaglom, A. M., 1987: *Correlation Theory of Stationary and Related Random Functions I*. Springer-Verlag, 512 pp.
- Yan, H., and R. A. Anthes, 1988: The effect of variations in the surface moisture on mesoscale circulations. *Mon. Wea. Rev.*, **116**, 192–208.